

# MAD about the Large Magellanic Cloud: ★ preparing for the era of Extremely Large Telescopes.

G. Fiorentino<sup>1,2</sup>, E. Tolstoy<sup>1</sup>, E. Diolaiti<sup>2</sup>, E. Valenti<sup>3</sup>, M. Cignoni<sup>2</sup>, & A. D. Mackey<sup>4</sup>

<sup>1</sup> Kapteyn Astronomical Institute, University of Groningen, PO Box 800, 9700 AV Groningen, The Netherlands.  
e-mail: fiorentino@astro.rug.nl

<sup>2</sup> INAF- Osservatorio Astronomico di Bologna, via Ranzani 1, 40127, Bologna, Italy.

<sup>3</sup> European Southern Observatory, Karl Schwarzschild-Straße 2, D-85748 Garching bei München, Germany.

<sup>4</sup> Research School of Astronomy & Astrophysics, Mount Stromlo Observatory, Cotter Road, Weston ACT 2611, Australia.

## ABSTRACT

We present J, H, K<sub>s</sub> photometry from the the Multi conjugate Adaptive optics Demonstrator (MAD), a visitor instrument at the VLT, of a resolved stellar population in a small crowded field in the bar of the Large Magellanic Cloud near the globular cluster NGC 1928. In a total exposure time of 6, 36 and 20 minutes, magnitude limits were achieved of J ~ 20.5 mag, H ~ 21 mag, and K<sub>s</sub> ~ 20.5 mag respectively, with S/N > 10. This does not reach the level of the oldest Main Sequence Turnoffs, however the resulting Colour-Magnitude Diagrams are the deepest and most accurate obtained so far in the infrared for the LMC bar. We combined our photometry with deep optical photometry from the Hubble Space Telescope/Advanced Camera for Surveys, which is a good match in spatial resolution. The comparison between synthetic and observed CMDs shows that the stellar population of the field we observed is consistent with the star formation history expected for the LMC bar, and that all combinations of IJHK<sub>s</sub> filters can, with some care, produce the same results. We used the Red Clump magnitude in K<sub>s</sub> to confirm the LMC distance modulus as,  $\mu_0 = 18.50 \pm 0.06$ ,  $\pm 0.09_s$  mag. We also addressed a number of technical aspects related to performing accurate photometry with adaptive optics images in crowded stellar fields, which has implications for how we should design and use the Extremely Large Telescopes of the future for studies of this kind.

**Key words.** AO–Near IR Technology–Resolved Stellar Population–LMC

## 1. Introduction

The presence of a wide variety of stellar populations of all ages makes the Large Magellanic Cloud (LMC) a rich laboratory to trace star-formation and evolution over a wide range of conditions and to calibrate several primary standard-candles for distance measurements. The LMC has been the subject of a number of ground breaking optical imaging studies with the Hubble Space Telescope (HST) of both field star population (e.g., Elson et al. 1997; Olsen 1999; Holtzman et al. 1999; Smecker-Hane et al. 2002) and the star clusters (e.g., Mackey & Gilmore 2004; Mackey et al. 2006) of a range of ages and metallicities. In particular, for the first time, accurate and detailed Colour-Magnitude Diagrams (CMDs) of star clusters located in the crowded region of the LMC bar (e.g. NGC 1928 and NGC 1939) were obtained (Mackey & Gilmore 2004).

A recent broader, although shallower, view comes from the wide field survey of Harris & Zaritsky (2009). The global star formation history (SFH) of the LMC is broadly consistent with that of its globular clusters. They show that the population of the LMC has an ancient component ( $\gtrsim 12$  Gyr old), which is followed by a quiescent period with very little star formation, after which there was a global episode of star formation which started about 5 Gyr ago. This last star formation peak may have been

caused by an interaction with SMC, and this intermediate age episode represents the bulk of the observed stellar population. These wide field results are also broadly consistent with deep HST CMDs (e.g., Holtzman et al. 1999, hereinafter H99; Olsen et al. 1999).

One of the main motivations for this study is that Extremely Large Telescopes (ELTs) are likely to be infrared (IR) optimised, using Adaptive Optics (AO) based instrumentation. This means that sensitive high-resolution ground-based imaging will only be possible at wavelengths starting from optical I-band, with a peak efficiency in the near-IR. Both sensitivity and spatial resolution are important for the study of resolved stellar populations, especially for compact galaxies and also for distances beyond the Local Group. Hence it is valuable to carry out pilot studies in this wavelength range with AO instruments available today.

Near-IR photometry does have several advantages: it can limit the effects of high and/or variable extinction in or towards a stellar field and it can also provide enhanced temperature sensitivity in a CMD, in particular when combined with optical bands. The optical-IR colour range stretches out most of the evolutionary features in a CMD making a unique interpretation more straight forward. However the use of only near-IR and I filters still needs to be properly investigated. At present stellar evolution theory is somewhat more uncertain in the near-IR, mostly due to the atmospheric models, and to a lack of accurate tests and calibrations over a wide age and metallicity range.

\* Based on observations obtained with the MCAO Demonstrator (MAD) at the VLT Melipal Nasmyth focus (ESO public data release).

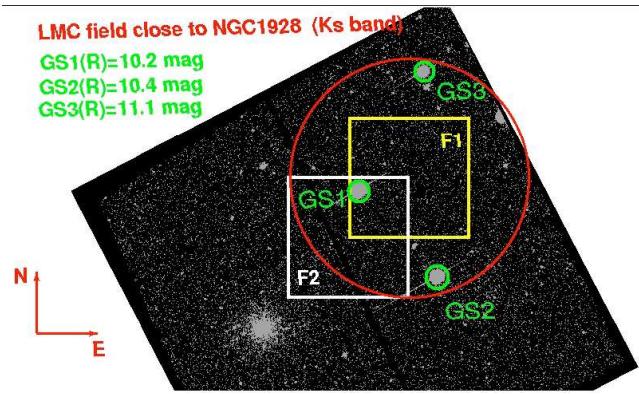


**Fig. 1.** An HST/ACS image in F555W band of the LMC field observed with MAD. The large (red) circle represents the entire MAD corrected field of view. This field is only partially covered by the detector, and the two observed fields F1 and F2 are indicated by squares. The three guide stars are indicated by small (green) circles (see Table 1 for details).

In this paper we present a data set that allows us to *i)* test the feasibility of carrying out accurate photometry of faint crowded stellar populations obtained with an MCAO system, and *ii)* to test theoretical models in the near-IR for intermediate age complex stellar populations. A simplistic study of the SFH of the observed field population has been performed first by using only our near-IR data, and then by combining them with HST/Advance Camera for Surveys (ACS) optical data. The consistency between optical and near-IR results is then discussed.

## 2. MAD Observations

MAD, the Multi-Conjugate Adaptive Optics (MCAO) Demonstrator<sup>1</sup>, is a prototype instrument built to prove the concept of MCAO using 3 natural guide stars. We were able to use it in the “star-oriented” wavefront sensing mode (Marchetti et al. 2006). In this mode MAD is equipped with three optical Shack-Hartmann wavefront sensors to measure the atmospheric turbulence from three guide stars located, ideally, at the vertices of an equilateral triangle within a field of 2 arcminutes diameter. MAD has also a “layer-oriented” wavefront sensing mode, built by INAF, and this mode may use up to 8 natural guide stars, which can be fainter than the guide stars in the star-oriented mode (see Momany et al. 2008; Gullieuszik et al. 2008; Moretti et al. 2009, for details). This mode was not offered for science demonstration observations.

The key advantage of MCAO is to increase the size and uniformity of the corrected field of view. MAD is able to probe the volume of atmospheric turbulence above the telescope by performing wavefront sensing on three natural guide stars, although successful observations have also been achieved with only two guide stars (Ferraro et al. 2009, M.H. Wong et al., in prep). Depending on the atmospheric seeing conditions, the limiting magnitude of the guide stars can be as faint as  $V \sim 13$  mag. These stars drive a tomographic reconstruction of the turbulence (Ragazzoni et al. 2000) carried out using two deformable mirrors conjugated at different altitudes in the atmosphere. CAMCAO is the MAD camera equipped with a  $2048 \times 2048$  pixel Hawaii2 IR detector with a pixel scale of 0.028 arcsec per pixel over a  $\sim 1$  arcmin square field. CAMCAO is mounted on

**Table 1.** Guide star positions and magnitudes.

STAR	$RA_{rel}^a$	$DEC_{rel}^a$	R (mag)
GS1	-19.4	-5	10.2
GS2	+15.3	-52.5	10.4
GS3	+19.6	-50.3	11.1

<sup>(a)</sup> The positions are given relative to the centre of the field ( $\alpha = 05^h 21^m 11^s$  and  $\delta = -69^\circ 27' 32''$  (J2000))

a movable table to be able to scan the full 2 arcminutes field if required. A standard set of J, H and  $K_s$  filters is available.

Science demonstration observations were carried out on UT3 at the VLT during three observing runs in 2007 and 2008. A number of studies of crowded stellar fields (mostly Galactic) have been published using this prototype system (e.g., Bono et al. 2009; Ferraro et al. 2009; Campbell et al. 2010; Sana et al. 2010). They achieve a spatial resolution that were previously only possible with space-based instrumentation.

MAD also provides the opportunity to understand the potential of future AO instrumentation on large telescopes (e.g., the European Extremely Large Telescope, E-ELT) to perform accurate photometric studies of distant resolved stellar populations. A number of E-ELT science cases assume that accurate photometry can be carried out at very faint levels over relatively wide fields of view with MCAO imagers. Thus, it is important to test the potential of such systems with currently available facilities. The photometry of point sources in crowded stellar fields is a useful, generally applicable, case which provides accurate probes of photometric sensitivity and depth over a wide field of view. Furthermore AO currently only works effectively at near-IR wavelengths and this is likely to remain the case for the foreseeable future. This implies adapting current CMD analysis techniques, which are almost exclusively carried out at optical wavelengths. These changes bring several challenges to be able to interpret these images and the first step is to obtain useful *training* data sets.

### 2.1. MAD Data

The MAD requirement of three bright natural guide stars within a circle of two arcmin of diameter combined with the need to image a region for which HST optical photometry was already available, limited the possible sky coverage. A suitable asterism was found in a region centered at  $\alpha = 05^h 21^m 11^s$  and  $\delta = -69^\circ 27' 32''$ , close to the LMC globular cluster NGC 1928. The area mapped by MAD observations is completely covered by ACS images of NGC 1928 (Mackey & Gilmore 2004). For wavefront sensing we used guide stars whose magnitudes and positions are listed in Table 1 and shown in Fig. 1. Using this asterism we observed two  $\sim 1' \times 1'$  fields (hereafter F1 and F2). As shown in Fig. 1, F1 is located at the center of the asterism and F2 is offset in a first attempt to get as close as possible to the globular cluster NGC 1928. F2 was observed, during the first run, to investigate the uniformity from the center to the edges of the  $2 \times 2$  arcmin field of view in the three J, H and  $K_s$  filters. During the second run we observed F1 and F2 (again) only in  $K_s$  filter. We did not manage to also observe F1 in J or H filters, and given that MAD was a test facility that was only on the telescope for a limited time it is not possible to rectify this. We thus present the best analysis we can with the data available.

During the first runs (Nov. 2007 and Jan. 2008), the LMC images were taken in J, H and  $K_s$  filters following a sequence of *SOOS OOSO*, where S is sky and O (science) object. The

<sup>1</sup> see also <http://www.eso.org/sci/facilities/develop/ao/sys/mad.html>

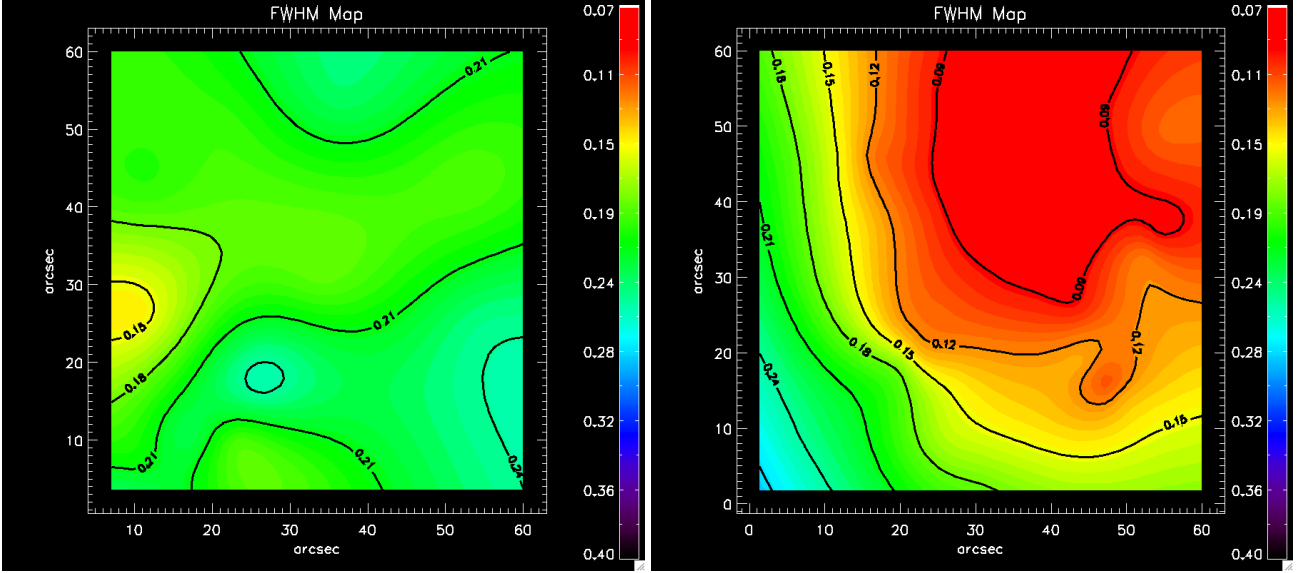


**Fig. 2.** The FWHM variation measured across the field F1 in  $K_s$  filter (left) and across the field F2 in H filter (right). The FWHM scale ranges from  $0.07''$  to  $0.5''$ , as is shown by the colour bars on the right. The (black) contours identify iso-density levels with a step of  $0.03''$ . **Left panel:** The FWHM is quite uniform varying from  $0.15''$  to  $0.24''$ . This field is well centered between the three guide stars. **Right panel:** The FWHM is very good ( $0.09''$ ) near the guide star GS1 (upper right hand corner), but the correction rapidly declines (down to  $0.24''$ ) towards the opposite corner.

final images are the combination of 42 J, 42 H and 60  $K_s$  exposures, each 10 sec long, resulting in the total exposure times shown in Table 2. The sky images have been taken in open loop (when the AO correction is switched off) offsetting the telescope several arcmins away and then applying a jitter pattern of  $\sim 5''$ . During the subsequent runs (Aug. 2008) we changed our strategy to minimize the observing time used for the sky acquisition, by obtaining sky directly from a series of jittered science images. A series of 60 images of  $10 \times 6$  sec were taken in  $K_s$  band, for a total exposure time equal to that of the previous run.

All images were processed using standard IR techniques, namely flat field normalization, dark and sky subtraction. A summary of the relevant technical information for all the observations is shown in Table 2. It was found that, due to rather unstable AO conditions, only a fraction of our images were ever of a quality suitable for photometric analysis (see section 2.3 for details), e.g. in  $K_s$  band this corresponds to an effective total exposure time of about 20 min out of 60 min of open shutter time. This means that an efficiency factor should always be taken into account when planning deep, sensitive images with high spatial resolution in AO-mode.

## 2.2. MAD Image Quality

One of the major issues in making deep AO images is obtaining and maintaining suitable image quality. Here we quantify the variation of MAD data in terms of image quality and we investigate the possible reasons.

### 2.2.1. Field Position relative to Guide Stars

We first estimated the stability of both the full width half maximum (FWHM) and the Strehl ratio (SR) of the Point Spread Function (PSF) across the observed fields, using an IDL program provided by E. Marchetti. Comparing the quality of the

correction with the diffraction limit<sup>2</sup> (DL), we see that we can use the H and  $K_s$  images of fields F1 and F2 interchangeably to study the AO performance across the MAD field of view. This is a reasonable approximation since the different SRs expected for H and  $K_s$  are quite well balanced by different atmospheric conditions of our observations.

Fig. 2 shows how the FWHM of the PSF varies for the best image in F1 ( $K_s$ , left panel) and F2 (H, right panel). In F1 there is a fairly uniform FWHM distribution across the whole field in comparison to F2. The uniformity of F1 meant that standard photometry techniques were straight forward to apply. In F2 however, the sharp changes at the edges of the field were more of a challenge

Despite the strong variation over the field, the best FWHM is achieved in F2 ( $0.08''$ ) and it is close to the H filter diffraction limit ( $0.05''$ ). In contrast, the uniform PSF in field F1 only reaches a FWHM of  $0.14''$ , which is twice the  $K_s$  diffraction limit ( $0.07''$ ). The mean FWHM is  $0.12''$  for H and  $0.20''$  for  $K_s$ . The Strehl Ratio (SR) shows a similar behaviour to the FWHM. The SR in field F1 is quite uniform with values ranging from 5 to 15%, whereas this distribution varies rapidly in field F2 from 5 to 25%. The maximum SRs obtained in both fields reach, or even exceed, the performances expected for MAD in “star-oriented” mode. The maximum SR was predicted to be between 11% to 24% for seeing ranging from  $0.7''$  to  $1.0''$ .

In conclusion, the uniformity of the PSF correction in the observed fields changes according to the different orientation with respect to the guide stars (see Fig. 1). A higher level of PSF uniformity, over the field of view is achieved within the central area enclosed by the asterism (in F1). However, the variations in peak and mean FWHM between observations are mostly due to different atmospheric conditions (see Table 2).

<sup>2</sup>  $DL(\lambda) \text{ (arcsec)} \sim \frac{1.22\lambda(\text{cm})}{D(\text{cm})} \times 206265 \text{ (arcsec)}$ . In the case of the VLT the DL is  $0.04''$  in J;  $0.05''$  in H;  $0.07''$  in  $K_s$ .

**Table 2.** Observation log: LMC field (close to NGC 1928).

Field ID	$RA_{rel}^a$	$DEC_{rel}^a$	filter	exptime (sec)	date	$\langle \text{airmass} \rangle$	$\langle \text{seeing} \rangle$
F1	0	0	$K_s$	3600	Aug 2008	1.65	0.45
F2	-25	-25	J	2520	Jan 2008	1.41	0.45
F2	-25	-25	H	2520	Jan 2008	1.41	0.55
F2	-25	-25	$K_s$	3600	Nov 2007	1.41	0.75
F2	-25	-25	$K_s$	3600	Aug 2008	1.68	0.65

<sup>(a)</sup> The positions are given relative to the centre of the field ( $\alpha=05^h21^m11^s$  and  $\delta=-69^\circ27'32''$  (J2000))

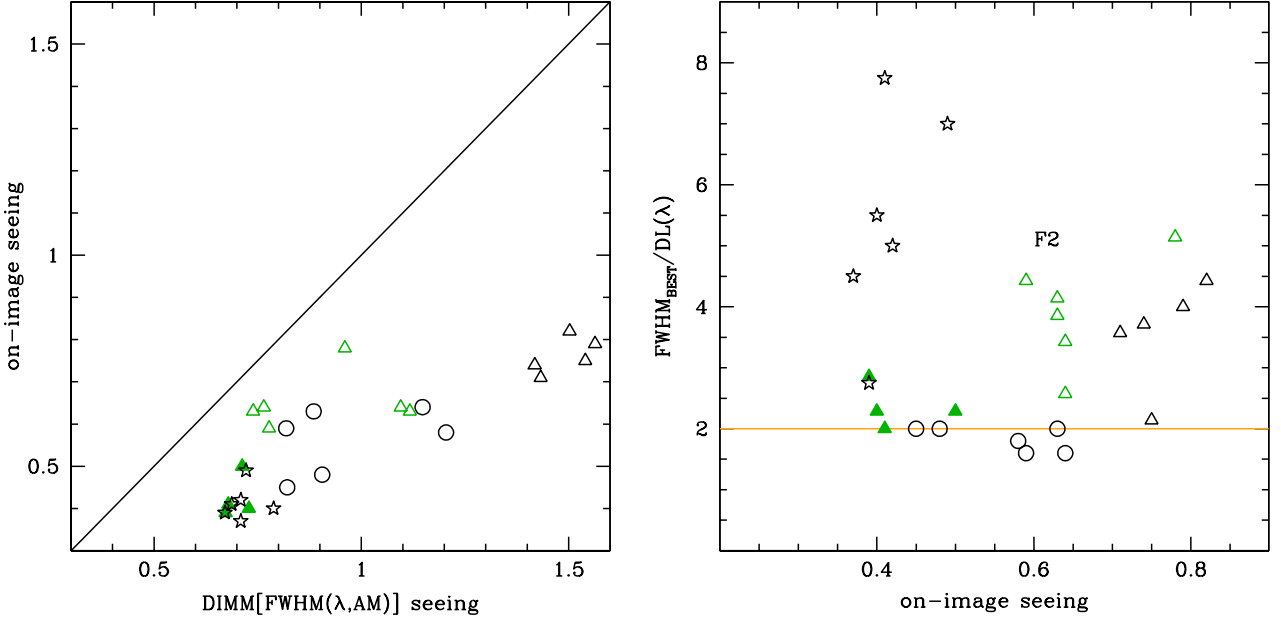


**Fig. 3.** Triangles, dots and stars represent  $K_s$ , H and J measurements, respectively. They are colour coded according to the airmass at which the observations were taken ( $\leq 1.5$  black;  $> 1.5$  green). Filled and empty symbols represent F1 and F2 images, respectively. **Left panel:** The seeing measured by the DIMM [FWHM( $\lambda$ ,AM)] scaled to the actual airmass and wavelength by using the standard relation given in the text is plotted against the FWHM measured on the sky images taken in open loop [ $FWHM_{sky}$ ], or on-image seeing]. **Right panel:** The ratio between the best FWHM of the Point Spread Function (PSF) measured in each image and the diffraction limit as a function of on-image seeing for the same data shown in the left panel. The solid (orange) line is 2 times the diffraction limit.

### 2.2.2. Airmass and Seeing

Many parameters, together with the target airmass and seeing, play a crucial role in the final AO performance. The most important are the absolute and relative magnitudes of the reference stars, the geometry of the asterism, the spatial extent of a turbulence cell (Fried's coherence length), the wavelength at which the correction is performed, and the vertical distribution of the atmospheric turbulence. As we do not have detailed information about the atmospheric parameters (e.g., the coherence length or the turbulence distribution) during the observations, we are only able to monitor the performance in terms of seeing and airmass. Hence, for a given asterism, we compare the FWHM measured against the telescope diffraction limit and the natural seeing.

It is well known that the seeing monitor on Paranal, the DIMM, gives systematically higher values, which are recorded in the image headers, than the true seeing measured on scientific images (Sarazin et al. 2008). Since we want to accurately quantify how the presence of the AO system affects the final images, we need reliable estimates of the natural seeing at the time of our observations. To do this we used the FWHM of stars measured on open loop sky images, which are uncorrected by the AO system and thus monitor the natural seeing. We have

checked for this effect by comparing our open loop images with the DIMM. The DIMM sensor uses optical filter and it monitors the atmosphere at zenith, hence we have used the standard formula  $FWHM(\lambda, AM) = DIMM(0.5/\lambda)^{1/5} \times AM^{3/5}$  (Sarazin 2003<sup>3</sup>) to derive the DIMM value at near-IR wavelengths and the target airmass. Fig. 3 (left panel) clearly shows that the DIMM always over-estimates the real seeing and the disagreement increases with the seeing.

Fig. 3 (right panel) shows the ratio of the best FWHM ( $FWHM_{BEST}$ ) in each image and the diffraction limit ( $DL(\lambda)$ ) as a function of the on-image natural seeing. Values around a factor 2 of the diffraction limit (solid line in the right panel of Fig. 3) are consistently achieved in  $K_s$  and H bands. Whereas in J (stars) the values are consistently much higher than 2 times the diffraction limit. As expected, the longer the observing wavelength, the better the AO performance. In our case the best correction was achieved for field F2 in H band (circles). This is probably due to the relatively low airmass of the H observations, compared to the  $K_s$ . For field F2 (and so, for a fixed asterism, empty symbols) and constant seeing, the main difference between H and  $K_s$  images is the airmass. This airmass effect can be balanced by a

<sup>3</sup> VLT-SPE-ESO-17410-1174

better relation between the field and the asterism. This can be seen, that F2 H images (empty circles) show a similar correction to F1  $K_s$  images (filled triangles), because the lower airmass of the H images compensates for the poorer AO correction.

Summarising, most of our data were obtained with an almost ideal triangular asterism with very bright guide stars (see Table 1). However it seems clear that to push the AO capabilities to faint limits and obtain optimum results, stringent observing constraints are needed. It is important to observe targets with an airmass  $\lesssim 1.5$  and/or with a seeing  $\lesssim 1$  arcsec. However it should also be noted that we almost always see a significant improvement with respect to natural seeing, of about a factor two, even for the unfavorable airmass at which the LMC was sometimes observed.

### 2.3. MAD Photometry

Photometry was performed using the standard data reduction package DAOPHOTIV/ALLSTAR and ALLFRAME provided by Stetson (1987, 1994). DAOPHOT/ALLSTAR models the PSF by the sum of a symmetric analytic bivariate function (typically a Lorentzian) and an empirical look-up table representing corrections to this analytic function from the observed brightness values within the average profile of several bright stars in the image. This hybrid PSF seems to offer adequate flexibility in modeling the complex PSFs that occur in real telescopes. Furthermore, the empirical look-up table makes it possible to account for the PSF variations (linear or quadratic) across the chip. This gives DAOPHOT/ALLSTAR the ability to carry out reliable photometry in many different circumstances, namely for standard ground based telescopes, the under sampled PSF of HST and also the complex PSFs of AO instruments.

We selected at least 100 isolated stars to estimate an analytical PSF for each frame. These stars were chosen to cover the whole field to account for the PSF variation. We then left DAOPHOT free to choose the analytic function that best fits the PSF shape requiring quadratic variations of the look-up table. ALLSTAR was used to perform photometry on each single frame. The resulting catalogues were used to align with DAOMATCH and DAOMASTER all the images in our reference star list, which is the optical catalog from HST/ACS. The near-IR images were then processed with ALLFRAME, which performs a second PSF-fitting by using the new, better defined, positions. ALLFRAME returns catalogues for each image that were combined using DAOMASTER to create the final photometric list.

If we compare the observed PSFs, and their variation over the field, with the PSF models created using DAOPHOT we see a good agreement. This comparison is shown in Fig. 4, for the challenging case of F2 in H band (see Fig. 2, right panel), where the residuals of the subtraction of the two distributions are shown. Fig. 4 shows how well the model follows the observed PSF distribution with only a few exceptions. The residuals are largest in the regions farthest from the guide stars, and where there are rapid changes in the observed PSF.

It is worth to mentioning that the PSF modeling and fitting procedure across the field turned out to be particularly easy thanks to the highly uniform AO correction provided by MAD. Accurate photometry with data acquired with a single conjugate AO (SCAO) system requires the use of complex highly variable PSFs, which require a combination of several Gaussians to take account of the strong variation in PSF shape across the image (see Origlia et al. 2008). This difference represents the major advantage that MCAO can provide.

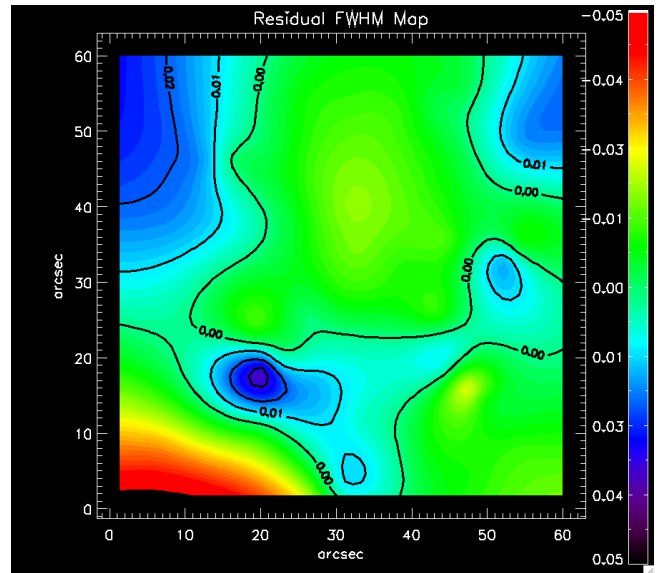


**Fig. 4.** The residual FWHM map from subtracting the observations of F2 in H band from the PSF model created using DAOPHOT.

The final matched photometry catalogues, containing 1218 and 1232 stars in fields F1 and F2, respectively, were obtained by cross-correlating the single-band catalogs using *CataXcorr* (P. Montegriffo, private communication) with *rms* residuals of  $\approx \pm 0.2''$ . There are  $\sim 140$  stars which have been observed in both F1 and F2, but only in  $K_s$ .

The instrumental magnitudes were converted to the Two Micron All Sky Survey (2MASS) photometric system, using 2MASS catalogues. Unfortunately, we found few stars in common between the two catalogues, due to the very different spatial resolution of MAD and 2MASS. This means that the comparison has a large overall uncertainty of  $\pm 0.10$  in J,  $\pm 0.19$  in H and  $\pm 0.09$  in  $K_s$ , in the zero-point calibration. By defining our limiting magnitude as the faintest magnitude with a S/N < 10, we reach: J  $\sim 20.5$  mag; H  $\sim 21$  mag;  $K_s \sim 20.5$  mag.

Most of our observations were taken in variable seeing conditions, and thus many individual images are not very sensitive due to poor S/N. To understand how our limiting magnitude corresponds to a total effective integration time we determined in how many images the stars at the limiting magnitude were detected. The number of these images times the exposure time for each image, has been considered as our ‘effective integration time’. From this definition, we used only 14% of the images in J band (corresponding to 6 mins of exposure time), 86% in H band (36 mins) and 33% of the images in  $K_s$  band.

### 3. HST/ACS Observations

The HST optical observations were taken during Cycle 12 using the ACS Wide Field Channel (WFC) centered at  $\alpha = 05^h 20^m 57^s$  and  $\delta = -69^\circ 28' 41''$ . Two exposures were taken through the F555W filter (330 s) and one through the F814W filter (200 s). The HST/ACS photometry has been carried out with DAOPHOT (in the IRAF environment) and is fully described by Mackey & Gilmore (2004). The HST/ACS photometry is very deep (at least 4 mag below the Main Sequence Turn Off (MSTO), i.e. V, I  $\sim 26$  mag) and the completeness is 100% at the level of our faintest IR observations. This optical catalogue was com-

bined with the JHK MAD catalogue, creating a final optical-IR catalogue of  $\sim 2600$  stars.

These optical data also allowed us to simply derive the completeness of our IR catalogue by matching the stars retrieved in the IR photometry to the complete HST photometry. Due to the large colour range (from  $V$  to  $K_s$ ) of our data set, the completeness has been derived independently for  $V-I > 0.75$  and  $V-I < 0.75$ . In the following analysis we used only stars with  $V$  magnitude brighter than 21 where both blue ( $V-I \leq 0.75$ ) and red ( $V-I > 0.75$ ) completeness values are higher than 50 %, in the three near-IR bands.

## 4. Results

### 4.1. The optical/IR CMDs

In Fig. 5 we show CMDs obtained from the optical-IR catalog with different filter combinations, most of which are likely to be possible with an imager on the E-ELT (e.g., Deep et al. 2011).

The best defined and most extended feature in an optical-IR CMD is of course the Red Giant Branch (RGB), see Fig. 5. The RGB signals the presence of stars  $\gtrsim 1$  Gyr old. It is notoriously difficult to interpret uniquely due to age-metallicity degeneracy effects. In all the CMDs in Fig. 5 there is also the clear presence of the Red Clump (RC), located at  $V \sim 19$  mag and at  $H, K_s \sim 17$  mag, which indicates the presence of intermediate and old stellar populations, in the range 1–10 Gyrs old. A blue plume shows the presence of young Main Sequence (MS) stars ( $< 100 - 500$  Myr old). A spread of stars just above the RC, is also clearly visible in Fig. 5, and is due to the presence of young blue loop stars. These can be useful to derive the metallicity of stellar populations  $\lesssim 1$  Gyr old (e.g., Dohm-Palmer et al. 1998).

As is clearly shown in Fig. 5, the combination of optical and IR filters stretches out the main CMD features, hence allowing an easier and more precise separation of different stellar populations in all evolutionary phases.

### 4.2. The Star Formation History

There exist robust techniques to make detailed analyses of observed CMDs by comparing them to theoretical models (e.g., Tosi et al. 1991; Tolstoy & Saha 1996; Aparicio et al. 1997; Dolphin 2002; Aparicio & Gallart 2004; Cignoni & Tosi 2010). From theoretical evolutionary tracks we know that in an optical-IR CMD the features will be stretched out due to the long colour baseline. However, although in the optical domain the theoretical stellar evolution models are well calibrated, in the near-IR they still have to be fully verified for a range of stellar evolution phases. Moreover this needs to be confirmed from an observational point of view using the actual photometric accuracies.

Here we present a basic application of the well established CMD synthesis methods to interpret our optical/IR CMDs in terms of a likely SFH. We start with a “known” SFH and see what are the effects of changing this. Given the uncertainties in the IR stellar evolution tracks we pay special attention to comparing the IR and IR+optical CMD results to the known SFH obtained with optical photometry alone.

Due to the limited depth and field of view of our IR photometry we cannot make a reliable determination of the SFH directly from our IR data. As a full SFH analysis from optical data already exists for a nearby LMC bar field, and within the errors of this kind of analysis, the optical CMDs are identical (see H99

& Mackey & Gilmore 2004), this allows us to directly compare our results to the careful and detailed SFH determined by H99.

We carry out a simple comparison, counting the number of stars falling in selected regions of the observed and theoretical CMDs for different filter combinations (as shown in Fig. 5); then we compute the probability that the chosen theoretical model (i.e., the synthetic CMD) matches our data.

We first recreated a synthetic population assuming the SFH and metallicity function from H99. This is our reference model (number 1 in Fig. 6, left panel). Then, we built 8 different populations, by changing the assumptions on both metallicity and age of the reference model. The variety of SFHs and the metallicity functions that have been explored are shown in Fig. 6 (left panel) with (red) lines and are compared to the H99 SFH (black) lines.

The models can be summarised as follows: 1) H99; 2) H99 without the old population; 3) H99 without the intermediate age population; 4) H99 without the very young population; 5) H99 with a very metal-poor and constant metallicity ( $Z=0.0001$ ); 6) Constant star formation rate (SFR), and constant low metallicity ( $Z=0.0001$ ); 7) H99 with a constant, high metallicity ( $Z=0.02$ ); 8) Constant SFR and constant, intermediate metallicity ( $Z=0.008$ ); 9) Constant SFR and constant, high metallicity ( $Z=0.02$ ).

The whole set of synthetic populations (each with one  $\sim 50\,000$  stars) have been simulated using the IAC-STAR (Aparicio & Gallart 2004), which generates synthetic CMDs for a given SFH and metallicity function. Composite stellar populations are calculated on a star-by-star basis, by computing the luminosity, effective temperature, and gravity of each star by interpolation in the metallicity and age grid of a library of stellar evolution tracks. We used the stellar evolution libraries of Girardi et al. (2000), the bolometric corrections libraries from Castelli & Kurucz (2001) and we assumed a Salpeter Initial Mass function. We fixed the reddening to  $E(B-V) = 0.075$  mag and the distance modulus to  $\mu_0 = 18.50$  mag, from H99. In order to compare our observations to theoretical models,  $K_s$  band magnitudes were transformed to the Bessell & Brett photometric system by adding 0.044 mag (see Salaris et al. 2003, and reference therein for details).

Finally, observational incompleteness and photometric errors are added to our synthetic CMDs, as derived from our data set, see Sec. 2.3 and Sec. 3. This allows us to compare the observations directly with the models. As an example, the simulated CMDs in  $I, I-K_s$  bands of the synthetic populations are shown in Fig. 6 (right panel). Similarly to Fig. 5, only stars with  $V \lesssim 21$  have been plotted and will be used in the following analysis, as they have a completeness  $> 50\%$  in the IR bands.

We briefly describe the main CMD features:

- Model 1) from H99, it has a very well populated MS, blue loop stars, and a compact RC where all ages are present;
- Model 2) is very similar to model 1, as it is only missing its old population that does not contribute much to the total number of stars at these magnitudes. The small cusp in the clump region of model 1 disappears in this model;
- Models 3-4) are missing the intermediate and young populations which are dominant in model 1, and the models can be excluded by eye as a good match to the data;
- Models 5-6) have a very low metallicity ( $Z=0.0001$ ) and are thus bluer than model 1 and their blue loop region is very extended;
- Models 7-9) with solar metallicity the RGB and the RC move to redder colours compared to model 1;

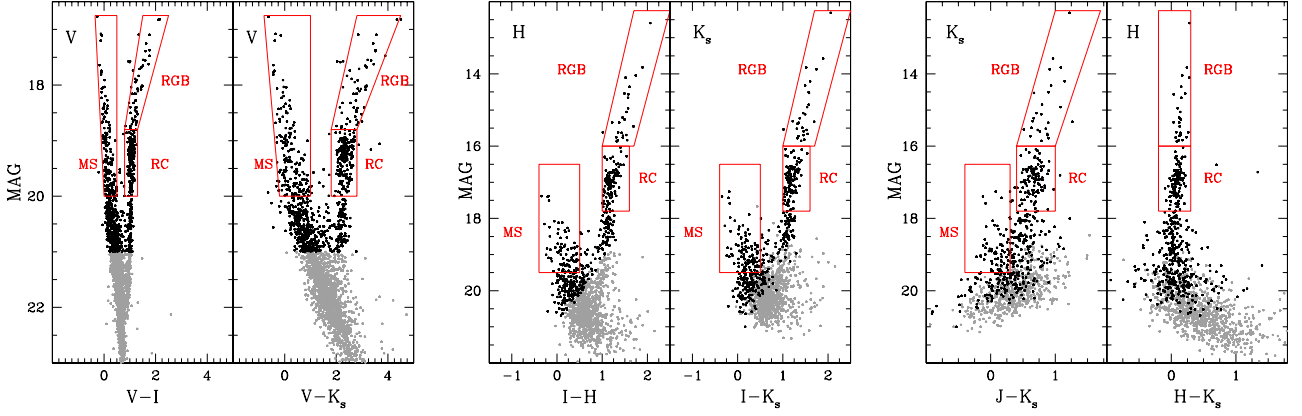


**Fig. 5.** The Colour-Magnitude Diagrams for our LMC bar field in different filter combinations. Starting from optical HST/ACS V, V-I (1st panel on the left), and extending to optical-IR, by adding MAD H and  $K_s$  photometry (central panels), and finally the MAD IR photometry alone (panels on the right). The grey points are all the sources found by Allframe and matched between different filters, and the black are only those with a completeness higher than 50% (see section 3). The boxes outline the main features of the CMDs, the Main Sequence (MS), the Red Giant Branch (RGB) and the Red Clump (RC).

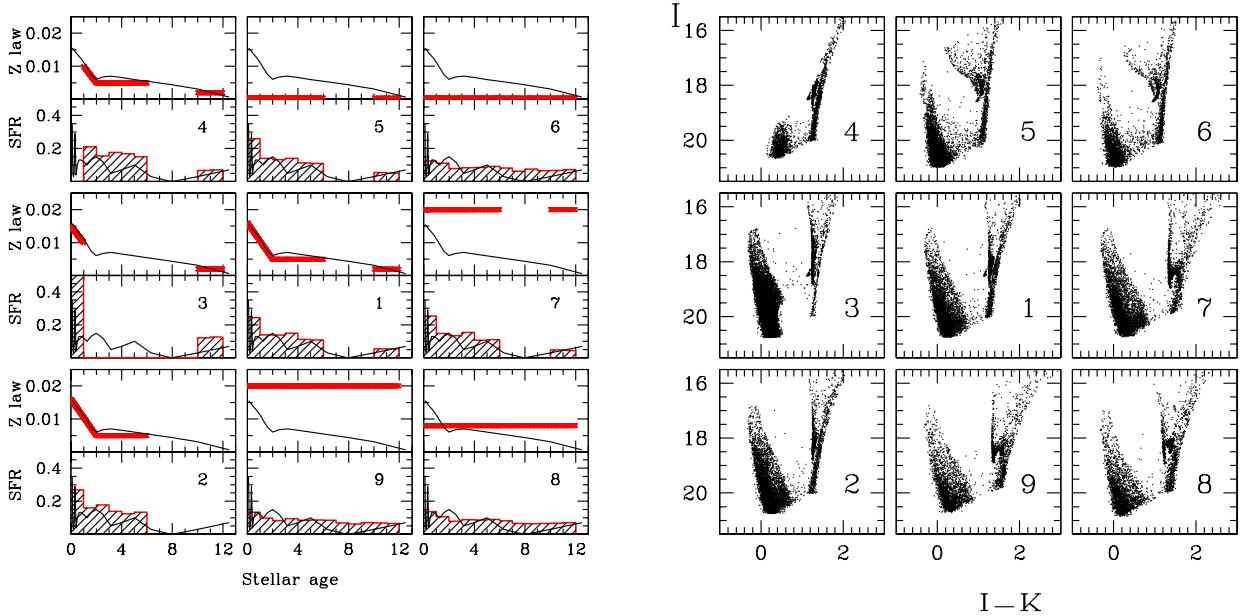


**Fig. 6.** **Left panel:** A series of synthetic SFH and metallicity functions are shown. The thin (black) lines are always the SFH and metallicity function of a field of the LMC bar, as derived from Holtzman et al. (1999). The thick (red) lines and the histograms show the values used to simulate the synthetic populations in order to find the best model that matches our observations. **Right panel:** Synthetic I, I- $K_s$  CMDs for different SFHs and metallicity functions, given in left panels. The number of the model is specified in each single panel as it is referred to in the text and in Tables 3 and 4.

- Model 8) is very similar to model 1, and the only difference is that a constant SFR results in a larger older population ( $\geq 6$  Gyr).

#### 4.2.1. Star counts

To compare the selected theoretical populations, shown in Fig. 6 (right panel), with our observations, we first counted the number of stars falling in the boxes (red) defined in Fig. 5. The ratio between the numbers of RC and MS stars to RGB stars for our models (labeled 1 - 9) relative to the observations have been plotted in Fig. 7 (left panel) for different filter combinations. The observed ratios for RC and MS are roughly the same for all the

filter combinations (see also Table 3), and an average of this (average) value is also shown (the solid line). We expect that the best matching models are able to reproduce the same ratio as the observations, lying very close to the solid line. Fig. 7 (left panel) shows that Models 8 and 5 are well matched to observations, whereas Model 1 is not. This shows that with these data we are not very well able to constrain the metallicity of the stellar population. However we are primarily interested in the self-consistency of the predictions made using different filter combinations.

The filter combinations shown here do give roughly the same information, and limitations. The only exception is the H- $K_s$  colour (red points in the left panel of Fig. 7), where the MS is

**Table 3.** The number of stars falling in the boxes outlined in Fig. 5, for different combination of filters. These boxes represent: Young (MS) and intermediate-old (RC and RGB) stellar populations.

N	MS (V-I)	RGB (V-I)	RC (V-I)	MS (V-K)	RGB (V-K)	RC (V-K)	MS (I-K)	RGB (I-K)	RC (I-K)	MS (I-H)	RGB (I-H)	RC (I-H)	MS (J-K)	RGB (J-K)	RC (J-K)	MS (H-K)	RGB (H-K)	RC (H-K)
Obs	183	52	195	175	53	190	151	46	197	86	26	111	83	24	100	2	2	2
1	2055	291	1176	2053	325	1176	1609	270	1297	1624	252	1292	1740	266	1298	29	29	29
2	2265	319	1195	2260	367	1195	1803	306	1337	1821	289	1335	1970	300	1337	33	33	33
3	5656	387	1093	5656	464	1092	4370	319	1330	4353	269	1364	4375	310	1333	36	36	36
4	54	209	1245	52	208	1245	130	196	1324	158	183	1321	310	196	1324	19	19	19
5	865	168	565	995	250	562	477	192	744	506	159	654	529	169	906	23	23	23
6	360	150	652	406	218	651	196	172	810	206	156	699	243	137	921	19	19	19
7	2156	210	1165	2140	172	1002	1746	171	1176	1757	258	1350	1947	309	1396	33	33	33
8	853	248	993	853	205	934	625	191	1110	632	221	1141	703	235	1165	23	23	23
9	891	113	980	882	86	801	763	85	965	776	157	1195	907	226	1302	23	23	23

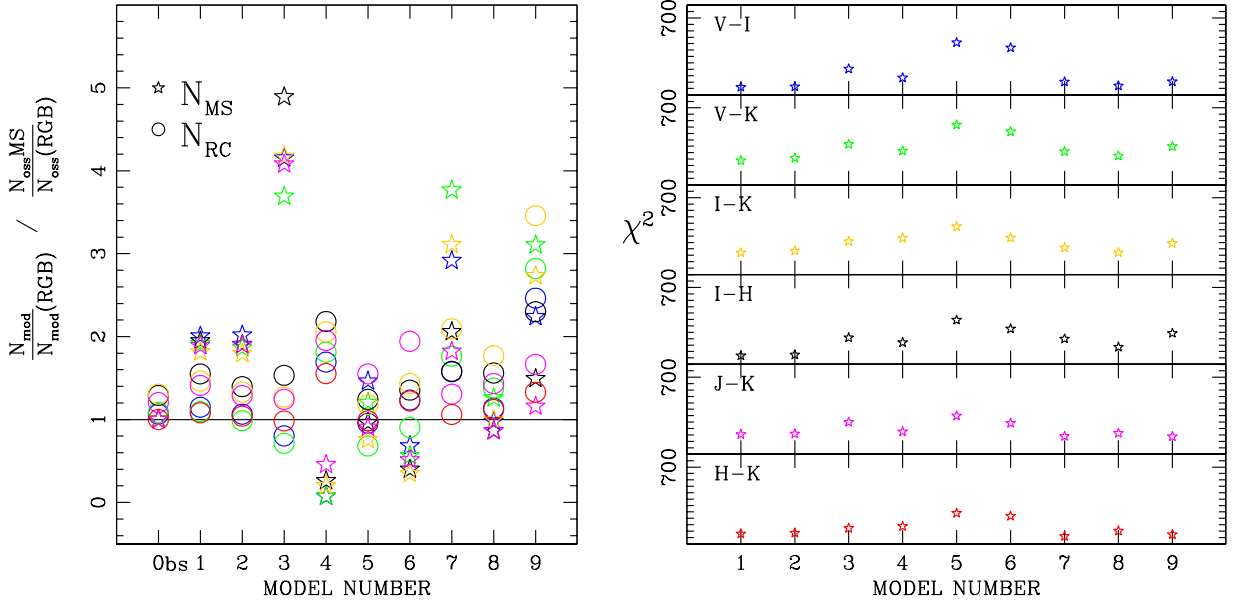


**Fig. 7.** **Left panel:** The ratio of the number of stars falling on the Main Sequence (MS, stars) and the Red Clump (RC, circles) to those on the RGB, as outlined in Fig. 5, for both observations and models for different filter combinations. These ratios have been normalized to the observed MS/RGB ratio. **Right panel** The  $\chi^2$  values for different combinations of filters for the set of models defined in Fig. 6, using a bin size of 0.15 in magnitudes and 0.25 in colour (see text for details). For this computation we have used only the stars in F2, with V, I, J, H and  $K_s$  photometry. **Both panels:** The colour code (only in the electronic version) is blue for V-I, green for V-K, yellow for I-K, black for I-H, magenta for J-K, and red for H-K.

missing. The MS can produce a clear distinction between different SFHs. However, in order to separate the MS from the RGB in H-K<sub>s</sub> colour ( $\leq 0.12$  mag from theoretical models) we would need a photometric error much smaller than 0.14 mag, which is our H-K<sub>s</sub> error, and it also excludes any systematics from the calibration. The J-K<sub>s</sub> colour (magenta points in the left panel of Fig. 7), works better, as the colour spread is estimated to be  $\sim 0.7$  mag.

#### 4.2.2. The $\chi^2$ Test

In this section we quantify our results using the  $\chi^2$  test in the form:

$$\chi^2 = \sum [m_i - n_i]^2 / [m_i + n_i] \quad (1)$$

where  $m_i$  and  $n_i$  are the number of stars falling in the bin  $i$ . This choice is made to account for the fact that both the theoret-

ical models ( $m$ ) and the observations ( $n$ ) are Poissonian distributions. In fact they are both random realizations of (unknown) distributions. As a consequence,  $\sigma_{m_i} = \sqrt{m_i}$  and  $\sigma_{n_i} = \sqrt{n_i}$ . We can normalize  $m_i$  to account for the fact that the total numbers of model and observed stars are not the same.

The choice of the bin size is crucial and is related to the photometric errors and the number of stars in individual bins. We investigated the possible dependence of our results on the bin size and adopted the most stable, which is a bin size of 0.15 in magnitude and 0.25 in colour. Moreover, to avoid introducing spurious effects we used only those stars with a completeness  $>50\%$  and observed in all VIJHK<sub>s</sub> filters, which means field F2.

The resulting  $\chi^2$  for each colour combination is shown in Fig. 7 (right panel). The best models matching our data are 1, 2 and 8 for almost all the filter combinations, the exceptions are J-K<sub>s</sub> and H-K<sub>s</sub>, for which the best models are 1, 2, 7, 8 and 9.

We can clearly see that all the colour combinations are able to confidently exclude models 5 and 6. This result is quite rea-



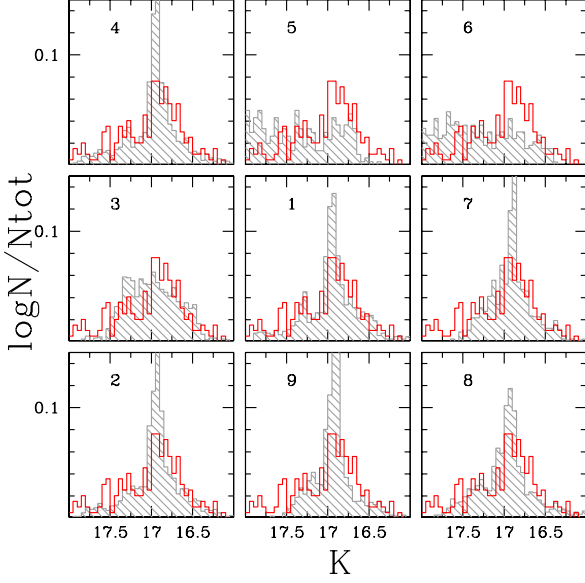


**Fig. 8.** Observed and model luminosity functions of the red clump region in  $K_s$  band, with a bin-size of 0.05 mag. The models, which are given in Fig. 6 (right panel), are shown as (grey) filled histograms and the data as (red) solid lines.

sonable for the range of magnitudes used ( $V \leq 21$ ), in fact we have considered only the brightest part of the CMD which increases the potential degeneracies in the SFH. Furthermore, the colour sensitivity, estimated as the maximum amplitude in the  $\chi^2$  distribution decreases from the top to the bottom panel of Fig. 7 (right panel), which is with increasing dependence on IR filters.

To summarise, the V–I CMD shows that the maximum sensitivity to the exact SFH comes from the HST/ACS optical data. This is mostly due to the very small photometric errors and the high completeness of this data set. It is also due to the greater reliability of the optical calibration of the stellar evolutionary tracks. We must also not forget that MAD is an experimental camera, with all the limitations that implies. It is nonetheless very encouraging that the optical/IR or purely IR  $\chi^2$  show the same trends, suggesting that the IR results could be improved, with deeper more accurate photometry and also reducing the uncertainties in the calibration of IR stellar evolution tracks. Thus, the standard techniques to determine the SFH of a galaxy are also applicable to our IR data. This suggests that we will also be able to collect useful data sets with extremely large telescopes, using broad-band filters, from I to  $K_s$ .

#### 4.3. The Red Clump

The RC feature is a well known and well studied distance indicator (see Girardi & Salaris 2001, and reference therein) in V, I and in particular the  $K_s$  filter. The distance of a galaxy based on its clump magnitude is calibrated on nearby clump stars whose distances are known with accurate *Hipparcos* trigonometric parallaxes (see first row in Table 1 in Salaris et al. 2003). Following Stanek & Garnavich (1998), given the histogram of stars in the clump region per magnitude bin (see Fig. 8), the apparent clump

**Table 4.** V, I and  $K_s$  band average de-reddened magnitudes of the RC stars and the corresponding distance modulus obtained by accounting for the population effect.

$\lambda$	$\lambda^{RC}$ (mag)	$\sigma_\lambda$ (mag)	$\mu_0(\lambda)$ (mag)
V	$18.98 \pm 0.04$	$0.26 \pm 0.04$	$18.51^a \pm 0.06_r$
I	$18.03 \pm 0.04$	$0.28 \pm 0.03$	$18.49^a \pm 0.06_r$
$K_s$	$16.93 \pm 0.04$	$0.38 \pm 0.04$	$18.50^a \pm 0.06_r \pm 0.09_s$

<sup>(a)</sup> SFH by (Holtzman et al. 1999) and the metallicity function from (Pagel & Tautvaisiene 1998), i.e. 0.26 mag, 0.20 mag and -0.03 mag for V, I and  $K_s$  band respectively (model Ia of Table 1 from Salaris et al. 2003).

magnitude ( $\lambda^{RC}$ ) is defined by performing a non linear least squares fit of the following function:

$$N(\lambda) = a + b\lambda + c\lambda^2 + d \exp - \frac{(\lambda^{RC} - \lambda)^2}{2\sigma_\lambda^2} \quad (2)$$

The accuracy of the mean clump magnitude is limited mainly by the photometric calibration of the data, rather than by the number of clump stars. Furthermore, as explained in detail by Girardi & Salaris (2001) the main concerns in the use of RC method to determine the distance are the extinction  $A_\lambda$  and population effects. A measurement in  $K_s$  is almost reddening independent.

The clump region was selected in colour and magnitude as shown in Fig. 5, and the resulting  $K_s$ -luminosity functions for both observation and models are shown in Fig. 8. Before computing the distance with the RC method, we want to stress that the observed luminosity function, the (red) solid histogram in Fig. 8, shows a blue tail for magnitudes fainter than the main clump magnitude ( $\sim 17.2$  mag). This substructure in the main clump is called the “secondary clump”. According to Girardi (1999) this is a clear signature of a population with age between 0.8–1.5 Gyr (see also right panel of Fig. 6). This can be particular useful when we are not able to reach the old main sequence turn-offs, as in the present case. To our knowledge this is the first time that a  $K_s$ -band photometry is accurate enough to clearly distinguish the secondary clump in the LMC.

The determination of the RC magnitudes are summarised in Table 4 with the corresponding distance modulus, derived by taking into account the metallicity-population correction given by Salaris et al. (2003) and assuming a reddening,  $E(B-V) = 0.075$  mag (H99). The errors on  $\lambda^{RC}$  and on  $\sigma_\lambda$  are those given by the non-linear fit, whereas the uncertainties on the derived distance moduli are: *i*) a random error which includes the errors from the fit (0.04 mag) and the photometry at the RC luminosity level (0.05 mag); *ii*) a systematic error on the calibration zero-point, which is non-negligible for the K-band (0.09 mag).

We found very similar values for the three filters V, I and  $K_s$ . The average for the three filters is  $\mu_0 = 18.50 \pm 0.06_r \pm 0.09_s$  mag, in excellent agreement with previous RC-based distances (Alves et al. 2002; Pietrzyński & Gieren 2002; Salaris et al. 2003). This is also in agreement with other independent methods in the literature such as Classical Cepheids, RR Lyrae and Planetary Nebulae luminosity functions, etc. (e.g. Bono et al. 2002; Catelan & Cortés 2008; Reid & Parker 2010). The models have been plotted in Fig. 8 by assuming a distance modulus of 18.5 mag, and they show a very good match to our observations in particular for models 1, 2 and 8 confirming the SFH results in this section.

## 5. Discussion and Conclusions

We have presented deep near-IR photometry from MAD on the VLT of the resolved stellar population in a small crowded field of the LMC bar. Using MAD in the star oriented mode, we have reached  $J \sim 20.6$  mag,  $H \sim 21.6$  mag, and  $K_s \sim 20.6$  mag with a S/N ratio  $> 10$  with *effective* exposure times of  $\sim 6$  mins in J,  $\sim 36$  mins in H and 20 mins in  $K_s$ .

The only comparable case of deep near-IR imaging of the LMC in literature is Pietrzyński & Gieren (2002) using NTT/SOFI. Their observations were taken with excellent seeing conditions (DIMM  $\sim 0.6$  arcsec) and at the lowest possible airmass ( $\sim 1.3$ ) from La Silla and over a large field of view of  $\sim 5$  arcmin square. Although our optical/near-IR CMDs look deeper, thanks to the high resolution offered by MAD/VLT and the addition of accurate optical photometry, the Pietrzyński & Gieren (2002) J–K CMD appears to have a better defined RC, due most likely to the large difference in the number of stars observed with the bigger NTT/SOFI field of view.

Taking advantage of these MAD data we have also analysed the image-quality. It should of course be born in mind that MAD was never optimised as a science instrument, it was always a demonstrator. Our main conclusions are summarised as follows:

- MAD has been able to reach twice the diffraction limit in H and  $K_s$  bands at the large zenith distances typical of the LMC. The maximum Strehl Ratio (SR) obtained is  $\sim 30\%$ , which is better than the expected performance for MAD in “star-oriented” mode. The uniformity and the stability of the correction varied not only with the position from the guide stars asterism, but also with airmass and seeing conditions. The complex dependency of these factors prevented us from making a direct comparison between our results and other MAD studies. However, in other experiments MAD was successfully able to reach the DL in  $K_s$  band (e.g. Falomo et al. 2009).
  - We quantified the constraints that appear to be necessary to push MAD capabilities to obtain optimum results from our observations. It would have been better to observe our target with an airmass  $< 1.5$  and DIMM less than  $< 1$  arcsec *to obtain results within at least a factor two of the diffraction limit for this system*. However it should also be noted that we see a significant improvement to natural seeing (around a factor 2) even for the unfavourable conditions under which the LMC was sometimes observed.
  - Another fundamental requirement for deep AO imaging is the ability to effectively co-add large numbers of measurements (made on individual images) to build up a final product that reaches faint magnitude limits with an angular resolution comparable to the diffraction limit. With current standard data reduction, image analysis and correction techniques we had to throw away a large fraction of our images (e.g.  $\sim 66\%$  in  $K_s$  filter). This could presumably be improved upon with clever post-processing techniques to correct images before analysing them. This may be achieved with the aid of PSF reconstruction techniques which should provide an accurate theoretical understanding of the form and variation of the PSF depending upon the atmospheric and instrumental variations. This would hopefully mean that less data need to be discarded during reduction and analysis, and thus providing deeper and sharper images.
  - The major and apparently unique advantage of MCAO, is that it can obviously provide a uniform AO correction over a wide field, allowing the straight forward use of the standard PSF modeling and fitting procedures.
- In our simplified scenario we assume that our data are identical to previously LMC bar results (Holtzman et al. 1999). Then, using our final optical/IR catalogue (VIJHK<sub>s</sub>), where the optical observations come from ACS/HST, we could determine how well stellar evolution models in the different filter combinations match our data for an assumed SFH (Holtzman et al. 1999). We conclude that we can be confident that the optical techniques for determining SFHs in V and I, can also be applied to IR data sets. Of course improvements in the calibration of IR isochrones would also be very helpful and are still needed.
  - From our RC analysis we derive a new, accurate, distance to the LMC:  $\mu_0 = 18.50 \pm 0.06_r \pm 0.09_s$  mag, assuming  $E(B-V) = 0.075$  mag. An inspection of the RC luminosity function confirms the evidence of the “secondary clump” feature in the  $K_s$ -band.

In conclusion, MAD is a demonstrator instrument with a small engineering grade detector, and yet the experiment worked very well. The future E-ELT will sample the atmospheric turbulence with a sampling step two times finer than MAD on VLT. This is just to stress that the peak correction achievable with MAD is smaller than that expected from the E-ELT. Thus some of the technical problems that we had with MAD, we would not expect with the E-ELT that will be much more stable in terms of uniformity and performance (e.g., Deep et al. 2011).

## Acknowledgments

We would like to thank the MAD team for useful suggestions during the preparation and carrying out of our observations, with particularly thanks to P. Amico and E. Marchetti. GF thanks M. Monelli for interesting discussions and for his help with IAC-STAR code, which has been used in this work. IAC-STAR is supported and maintained by the computer division of the Instituto de Astrofísica de Canarias. We thank the anonymous referee for invaluable help clarifying the results presented in this paper.

This publication makes use of data products from the Two Micron All Sky Survey, which is a joint project of the University of Massachusetts and Infrared Processing and Analysis Center/California Institute of Technology, funded by the National Aeronautics and Space Administration and the National Science Foundation. ET & GF have been supported by an NWO-VICI grant.

## References

- Alves, D. R., Rejkuba, M., Minniti, D., & Cook, K. H. 2002, ApJ, 573, L51  
Aparicio, A. & Gallart, C. 2004, AJ, 128, 1465  
Aparicio, A., Gallart, C., & Bertelli, G. 1997, AJ, 114, 680  
Bono, G., Calamida, A., Corsi, C. E., et al. 2009, in Science with the VLT in the ELT Era, ed. A. Moorwood, 67–+  
Bono, G., Castellani, V., & Marconi, M. 2002, ApJ, 565, L83  
Campbell, M. A., Evans, C. J., Mackey, A. D., et al. 2010, MNRAS, 405, 421  
Castelli, F. & Kurucz, R. L. 2001, A&A, 372, 260  
Catelan, M. & Cortés, C. 2008, ApJ, 676, L135  
Cignoni, M. & Tosi, M. 2010, Advances in Astronomy, 2010  
Deep, A., Fiorentino, G., Tolstoy, E., et al. 2011, A&A, 531, A151+  
Dolphin, A. E. 2002, MNRAS, 332, 91  
Elson, R. A. W., Gilmore, G. F., & Santiago, B. X. 1997, MNRAS, 289, 157  
Falomo, R., Pian, E., Treves, A., et al. 2009, A&A, 501, 907  
Ferraro, F. R., Dalessandro, E., Mucciarelli, A., et al. 2009, Nature, 462, 483  
Girardi, L. 1999, MNRAS, 308, 818  
Girardi, L., Bressan, A., Bertelli, G., & Chiosi, C. 2000, A&AS, 141, 371  
Girardi, L. & Salaris, M. 2001, MNRAS, 323, 109  
Gullieuszik, M., Greggio, L., Held, E. V., et al. 2008, A&A, 483, L5  
Harris, J. & Zaritsky, D. 2009, AJ, 138, 1243

- Holtzman, J. A., Gallagher, III, J. S., Cole, A. A., et al. 1999, *AJ*, 118, 2262
- Mackey, A. D. & Gilmore, G. F. 2004, *MNRAS*, 352, 153
- Mackey, A. D., Payne, M. J., & Gilmore, G. F. 2006, *MNRAS*, 369, 921
- Marchetti, E., Brast, R., Delabre, B., et al. 2006, in Presented at the Society of Photo-Optical Instrumentation Engineers (SPIE) Conference, Vol. 6272, Society of Photo-Optical Instrumentation Engineers (SPIE) Conference Series
- Momany, Y., Ortolani, S., Bonatto, C., Bica, E., & Barbuy, B. 2008, *MNRAS*, 391, 1650
- Moretti, A., Piotto, G., Arcidiacono, C., et al. 2009, *A&A*, 493, 539
- Olsen, K. A. G. 1999, *AJ*, 117, 2244
- Pagel, B. E. J. & Tautvaisiene, G. 1998, *MNRAS*, 299, 535
- Pietrzyński, G. & Gieren, W. 2002, *AJ*, 124, 2633
- Ragazzoni, R., Marchetti, E., & Valente, G. 2000, *Nature*, 403, 54
- Reid, W. A. & Parker, Q. A. 2010, *MNRAS*, 716
- Salaris, M., Percival, S., & Girardi, L. 2003, *MNRAS*, 345, 1030
- Sana, H., Momany, Y., Gieles, M., et al. 2010, *A&A*, 515, A26+
- Sarazin, M., Melnick, J., Navarrete, J., & Lombardi, G. 2008, *The Messenger*, 132, 11
- Smeecker-Hane, T. A., Cole, A. A., Gallagher, III, J. S., & Stetson, P. B. 2002, *ApJ*, 566, 239
- Stanek, K. Z. & Garnavich, P. M. 1998, *ApJ*, 503, L131+
- Stetson, P. B. 1987, *PASP*, 99, 191
- Stetson, P. B. 1994, *PASP*, 106, 250
- Tolstoy, E. & Saha, A. 1996, *ApJ*, 462, 672
- Tosi, M., Greggio, L., Marconi, G., & Focardi, P. 1991, *AJ*, 102, 951